Half-vortex sheets and domain-wall trains of rotating two-component Bose-Einstein condensates in spin-dependent optical lattices

Wei Han,[1,2] Suying Zhang,[1,*] Jingjing Jin,[1] and W. M. Liu[2]

[1]*Institute of Theoretical Physics, Shanxi University, Taiyuan 030006, China*

[2]*Beijing National Laboratory for Condensed Matter Physics, Institute of Physics, Chinese Academy of Sciences, Beijing 100190, China*

(Received 27 December 2011; revised manuscript received 9 April 2012; published 30 April 2012)

We investigate half-vortex sheets and domain-wall trains of rotating two-component Bose-Einstein condensates in spin-dependent optical lattices. The two-component condensates undergo phase separation in the form of stripes arranged alternately. The vortices of one component are aligned in lines in the low-density regions and filled with the other component, which results in a stable vortex configuration, straight half-vortex sheets. A train of domain walls, with spatially periodic eyebrowlike spin textures embedded on them, are formed at the interfaces of the two components. We reveal that these spatially periodic textures on the domain walls result from the linear gradient of the relative phase, which is induced by the alternating arrangement of the vortex sheets in the two components. An accurate manipulation of the textures can be realized by adjusting the intercomponent interaction strength, the rotating angular frequency, and the period of the optical lattices. Under external disturbances, some interesting phenomena, including collective movement of vortices along the sheets and spin-wave propagation along the domain walls, as well as local spin precession, are observed.

DOI: 10.1103/PhysRevA.85.043626 PACS number(s): 03.75.Mn, 03.75.Lm, 67.85.Hj, 03.75.Hh

I. INTRODUCTION

Topological excitations, such as quantized vortices, domain walls, and textures, exist in many fields of physics, and have attracted much interest of physicists. In cosmology, topological excitations are theoretically predicted to play an important role in structure formation in the early Universe. Quantized vortices have been observed experimentally in type-II superconductors, liquid helium, and atomic gases Bose-Einstein condensates (BECs). In contrast to classical vortices, as the unique advantages in identifying and simulating, quantized vortices provide the possibility of understanding and controlling quantum turbulence [1]. Domain walls, which are the interfaces separating magnetic domains, have been systematically investigated in magnetism and magnetic materials. Recent research has shown that domain wall has potential application prospect in the racetrack memory, which is believed to bring the revolution of information storage technology [2]. Textures, such as skyrmions, have also been observed in magnetic materials [3], and will become favorites of information processing and storage [4].

BECs provide an ideal impurity-free environment for the research of topological excitations. At the same time, topological excitations play an essential role in understanding superfluidity and magnetism of BECs. In a single-component BEC, topological excitations manifest themselves as integer vortices [5–8]. Multicomponent BECs, which are described by a vector order parameter, allow the existence of more variety of exotic topological excitations, such as fractional vortices [9–13], domain walls [9,14–19], and textures [9,20–24].

BECs respond to rotation by creating quantized vortices. In different rotation systems or different parameter regions of the same system, vortices usually arrange themselves as different structures, which reflect different features of superfluidity in a quite visually intuitive way. In a rotating single-component condensate, the vortex structure is relatively simplistic, vortices always prefer to arrange themselves as a regular Abrikosov triangular lattice [25]. Unlike the case in single-component BECs, the vortex structures in two-component BECs are very rich.

When the atomic masses, the particle numbers, and the intracomponent interaction strengths are approximately equal, the vortex structure in two-component BECs roughly depends on the intercomponent interaction strength [26–31]. In the case of negative intercomponent interaction, it is energetically favorable for the vortices to form an overlapped Abrikosov triangular lattice [26]. With increasing the strength of intercomponent interaction from zero, the positions of vortex cores in one component gradually shift from those of the other component and form an interlaced triangular lattice [26,27]. With the intercomponent interaction strength further increasing, the interlaced triangular lattice is deformed into an interlaced square lattice [26–28]. If the intercomponent and intracomponent interaction strengths are nearly equal, the vortex structure evolves into straight vortex sheets, which are made up of alternating straight chains of vortices of each component [27,29,30]. When the intercomponent interaction is stronger that the intracomponent interaction, the straight vortex sheets bend and are replaced by serpentine vortex sheets [30]. In the limit of intercomponent interaction, the system eventually evolves rotating droplets, where the components are completely phase separated and each component contains a single patch of density [30,31].

When the particle numbers of the two components are unequal, one component is surrounded by the other component, and a giant vortex can be formed in the outer component [31,32]. In addition, considering the case of large atomic mass ratios of the two components, more exotic vortex structures, such as a two-quantum vortex lattice [33], would be obtained.

*zhangsy@sxu.edu.cn

The arrangement of vortices plays an important role in creating various spin texture patterns, which are intuitive reflections of the magnetism of multicomponent BECs. Generally speaking, different vortex configurations always correspond to different kinds of spin textures. For example, an Anderson-Toulouse vortex and Mermin-Ho vortices correspond to a skyrmion and a meron pair, respectively [34,35], and a pair of vortices with opposite signs that reside in different components correspond to a spin-2 texture [21]. This suggests that it is a feasible method to produce more various spin textures by controlling the arrangement of the vortices. As the sophisticated experimental technology of the manipulation and observation of BECs, both the vortex structures and spin textures can be well manipulated and observed in the experiment.

In this paper, we study the vortex structures of rotating two-component BECs in one-dimensional (1D) spin-dependent optical lattices, which have not yet been studied. We find that this system supports a stable vortex structure, straight half-vortex sheets, which are made up of straight chains of half quantized vortices. The vortex sheets of the two components are arranged alternately and each sheet in one component is filled with the other component, which results in alternately arranged density stripes. As mentioned above, similar structure has also been observed in the pure harmonic trap. However, in that case, the parameter region of this phase is extremely narrow. At the same time, that structure is unstable, as there exist many different metastable bent vortex sheet configurations with almost the same energy as the straight one. In contrast, as the presence of the spin-dependent optical lattices, this structure is robust with respect to external disturbances. Moreover, it does not face the intracomponent interaction strength limitations.

A dramatic characteristic of this structure is its unique superfluid velocity behavior. The tangential component, which is the component along the sheet direction, of the superfluid velocity always discontinuously jumps across every sheet. We give a quantitative description of this behavior both analytically and numerically.

Besides vortex, this system supports another kind of topological excitation, domain wall. As the presence of the spin-dependent optical lattices, the two-component BECs are phase separated and a train of domain walls are formed naturally at their interfaces. By describing the system in terms of pseudospin density parameters, we investigate the response of the domain walls to external rotation. It is found that in the absence of rotation, the domain walls are classical Néel walls, with the magnetic moments only reversing perpendicular to the walls, while in the presence of rotation, the magnetic moments on the domain walls twist and form spatially periodic eyebrowlike spin textures.

This eyebrowlike spin texture has the same topological charge as a skyrmion, but their structures are distinctly different. We described the structure of this spin texture in detail by projecting it on a Bloch sphere. We reveal the formation mechanism of the eyebrowlike spin textures and discuss the influences of the system parameters on their distribution. An exact expression on the number of the textures carried by a domain wall is given, which provides us a promising way to create and manipulate spin textures in BECs.

We also study the dynamics of this system under external disturbances. The stability of the straight half-vortex sheets is proved by real-time dynamical evolution. At the same time, we observe some interesting dynamical phenomena, including collective movement of vortices along the sheets and spin-wave propagation along the domain walls, as well as local spin precession.

This paper is organized as follows. In Sec. II, we give the model of the rotating two-component BECs in spin-dependent optical lattices. In Sec. III, we study the stable straight half-vortex sheet structure, and discuss its unique superfluid velocity behavior. In Sec. IV, we investigate the internal structure of the domain walls and its response to external rotation, and reveal the formation mechanism of the spatially periodic eyebrowlike spin textures. In Sec. V, we focus on the influences of the system parameters on the spin textures. The dynamical behaviors of this system under external disturbances are discussed in Sec. VI. We conclude this paper in Sec. VII.

II. MODEL

We consider two-component BECs with two hyperfine spin states. In the weak interaction limit, the two-component condensates in a frame rotating at an angular frequency Ω around the z axis can be described by the coupled Gross-Pitaevskii (GP) equations

$$i\hbar\frac{\partial\Psi_i(\mathbf{r},t)}{\partial t}=\left[-\frac{\hbar^2}{2m}\nabla^2+V_{\mathrm{H}}+\sum_{j=1,2}g_{ij}|\Psi_j|^2+V_{\mathrm{OL}i}-\Omega\hat{L}_z\right]\Psi_i(\mathbf{r},t), \tag{1}$$

where Ψ_i is the macroscopic wave function of the ith component ($i=1,2$). $g_{ij}=4\pi\hbar^2a_{ij}/m$ represents the strength of interatomic interactions characterized by the intracomponent and intercomponent s-wave scattering lengths a_{ij} and the mass m of an atom. $\hat{L}_z=-i\hbar(x\partial_y-y\partial_x)$ is the z component of the angular momentum operator. The external potential consists of two parts, the harmonic trapping potential $V_{\mathrm{H}}=\frac{1}{2}m[\omega_\perp^2(x^2+y^2)+\omega_z^2z^2]$ and the spin-dependent optical lattice potential $V_{\mathrm{OL}i}$, where $V_{\mathrm{OL}1}=I_0\sin^2(kx)$ and $V_{\mathrm{OL}2}=I_0\cos^2(kx)$. Here k is the wave vector of the laser light used for the optical lattice potentials and I_0 is the potential depth of the lattices. The wave functions are normalized as $\sum_i\int|\Psi_i|^2d\mathbf{r}=N$, where N is the total number of condensate atoms.

For simplicity, we assume that the harmonic trapping frequencies satisfy $\omega_z\gg\omega_\perp$. Then, the condensates are pressed into a pancake. This allows us to reduce Eq. (1) to a two-dimensional form as [36]

$$i\hbar\frac{\partial\psi_i(x,y,t)}{\partial t}=\left[-\frac{\hbar^2}{2m}\nabla^2+\tilde{V}_{\mathrm{H}}+\sum_{j=1,2}\eta g_{ij}|\psi_j|^2+V_{\mathrm{OL}i}-\Omega\hat{L}_z\right]\psi_i(x,y,t), \tag{2}$$

where $\eta=(h/m\omega_z)^{-1/2}$ is a reductive parameter. The two-dimensional wave functions are normalized as

$\sum_i \int |\psi_i|^2 dxdy = N$. The harmonic trapping potential is reduced to its 2D form $\tilde{V}_{\rm H} = \frac{1}{2}m\omega_\perp^2(x^2+y^2)$, where the tilde will be omitted in the following discussions for simplicity.

For numerical calculations, it is convenient to make the following parameter transformations,

$$\begin{aligned} &x = a_h\tilde{x}, \quad y = a_h\tilde{y}, \quad t = \tilde{t}\omega_\perp^{-1}, \\ &k = \tilde{k}a_h^{-1}, \quad I_0 = \tilde{I}_0\hbar\omega_\perp, \quad \Omega = \omega_\perp\tilde{\Omega}, \\ &\psi_i = N^{1/2}a_h^{-1}\tilde{\psi}_i, \quad \beta_{ij} = 4\pi N\eta a_{ij}, \end{aligned} \tag{3}$$

where $a_h = \sqrt{\hbar/m\omega_\perp}$ is the characteristic length of the harmonic trap. Then the two-dimensional GP equation Eq. (2) is reduced to a dimensionless form as

$$i\frac{\partial\tilde{\psi}_1}{\partial\tilde{t}} = \left[-\frac{1}{2}\tilde{\nabla}^2 + \frac{1}{2}(\tilde{x}^2+\tilde{y}^2) + \sum_{j=1,2}\beta_{1j}|\tilde{\psi}_j|^2 + \tilde{I}_0\sin^2(\tilde{k}\tilde{x}) + i\tilde{\Omega}(\tilde{x}\partial_{\tilde{y}} - \tilde{y}\partial_{\tilde{x}})\right]\tilde{\psi}_1, \tag{4a}$$

$$i\frac{\partial\tilde{\psi}_2}{\partial\tilde{t}} = \left[-\frac{1}{2}\tilde{\nabla}^2 + \frac{1}{2}(\tilde{x}^2+\tilde{y}^2) + \sum_{j=1,2}\beta_{2j}|\tilde{\psi}_j|^2 + \tilde{I}_0\cos^2(\tilde{k}\tilde{x}) + i\tilde{\Omega}(\tilde{x}\partial_{\tilde{y}} - \tilde{y}\partial_{\tilde{x}})\right]\tilde{\psi}_2, \tag{4b}$$

where β_{ij} represents the 2D dimensionless effective interaction parameters, determined by the s-wave scattering lengths, the total number of condensate atoms, and the axial trapping frequency. The two-dimensional dimensionless wave functions are normalized as $\sum_i \int |\tilde{\psi}_i|^2 d\tilde{x}d\tilde{y} = 1$.

In order to describe the system more clearly, the intuitive pictures of the external potentials are presented in Figs. 1(a)–1(f). Experimentally, the spin-dependent optical lattice potentials $V_{\rm OL1}$ and $V_{\rm OL2}$ can be realized by employing two counterpropagating blue-detuned laser beams with the same frequency but perpendicular linear polarization vectors [37]. A schematic of the spin-dependent optical lattices is presented in Fig. 1(g).

In our simulations, stemming from the consideration of experiments, we choose a two-level ^{87}Rb BEC system with $|F=1, m_f=-1\rangle \equiv |1\rangle$ and $|F=2, m_f=1\rangle \equiv |2\rangle$ [38]. The ^{87}Rb atoms are assigned to the two states equally and the total number of them is $N = 10^5$. The radial and axial trapping frequencies are $\omega_\perp = 2\pi \times 15$ Hz and $\omega_z = 2\pi \times 150$ Hz, respectively. We use the scattering lengths [38]: $a_{11} = 100.40a_0$, $a_{22} = 95.00a_0$, and $a_{12} = a_{21} = 97.66a_0$ (a_0 is the Bohr radius), except when we discuss the influence of the intercomponent interaction on the textures in Sec. V. The intensity of the laser light used for the optical lattice potentials is chosen as $I_0 = k_B \times 27.5$ nK (k_B is the Boltzmann's constant) [39], which is powerful enough such that the two states are phase separated. With these experimental parameters, according to the transformation relation Eq. (3), we can calculate the corresponding computational parameters for our numerical simulations as: $\beta_{11} = 3025$, $\beta_{22} = 2862$, $\beta_{12} = \beta_{21} = 2942$, and $\tilde{I}_0 = 38.2$.

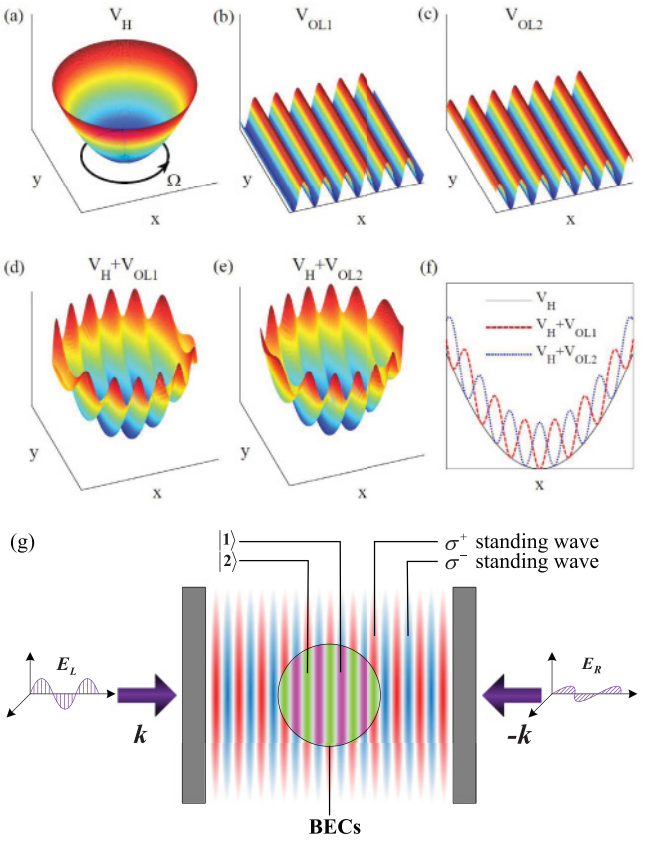

FIG. 1. (Color online) (a) The harmonic trapping potential $V_{\rm H}$ is rotated about the z axis at a frequency Ω. (b) The spin-dependent optical lattice potential $V_{\rm OL1} = I_0\sin^2(kx)$, which is experienced by the $|1\rangle$ state. (c) The spin-dependent optical lattice potential $V_{\rm OL2} = I_0\cos^2(kx)$, which is experienced by the $|2\rangle$ state. (d) The composite potential $V_{\rm H} + V_{\rm OL1}$. (e) The composite potential $V_{\rm H} + V_{\rm OL2}$. (f) Cross sections of $V_{\rm H}$ (solid line), $V_{\rm H} + V_{\rm OL1}$ (dashed line), and $V_{\rm H} + V_{\rm OL2}$ (dotted line) along the x axis. (g) Schematic of the spin-dependent optical lattices. Two polarized standing wave laser fields σ^+ (red) and σ^- (blue) are formed by two counterpropagating blue-detuned laser beams with the same frequency but perpendicular linear polarization vectors. This gives rise to the optical lattice potentials $V_{\rm OL1}$ and $V_{\rm OL2}$, which are experienced by the $|1\rangle$ state (pink) and the $|2\rangle$ state (green), respectively.

III. HALF-VORTEX SHEETS

In this section, we present a stable vortex configuration, straight half-vortex sheets. By using the imaginary-time propagation method [40,41], we solve Eq. (4) numerically and obtain the ground state of the two-component condensates. Without loss of generality, we choose the rotating angular frequency $\Omega = 0.6\omega_\perp$ and the period of the optical lattice potential $T = \pi\xi$, where $\xi = (\hbar/m\omega_\perp)^{-1}$ is the spatial scale. The density profiles are presented in Fig. 2. All the vortices are denoted by crosses ($\times$), whose positions are determined by the singularities of the phase. As the presence of the spin-dependent optical lattices, the two-component condensates undergo phase separation in the form of stripes arranged alternately. It is energetically favorable for the vortices to site in the low-density regions, so we find that all the vortices of one component are aligned in lines in the trough of the

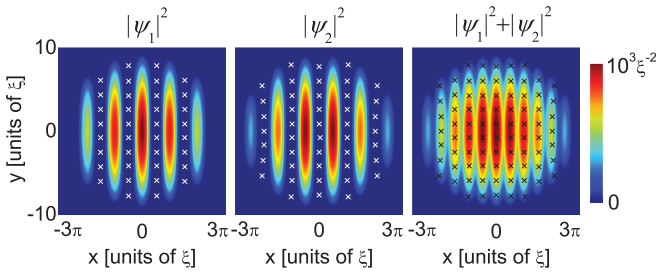

FIG. 2. (Color online) The ground state density profiles of $|\psi_1|^2$, $|\psi_2|^2$, and $|\psi_1|^2 + |\psi_2|^2$ for the rotating angular frequency $\Omega = 0.6\omega_\perp$ and the period of the optical lattice potential $T = \pi\xi$ with $\xi = (\hbar/m\omega_\perp)^{1/2}$. The locations of the vortices are marked by crosses (×).

optical lattice potential and filled with the other component. This results in alternately arranged straight vortex sheets in the two components. Obviously, all the positions of the vortices in one component are vortex-free regions in the other component, so all the vortices are half quantized [11–13]. We refer to this vortex configuration as straight half-vortex sheets. It should be indicated that the rotational frequency Ω for the realization of the straight half-vortex sheets is not limited to $0.6\omega_\perp$, but it can take the value from 0 to $\omega_\perp$. Even though the half-vortex sheets do not influence the total density distribution of the condensates, they are crucial for the formation of the spatially periodic spin textures on the domain walls.

In the absence of the spin-dependent optical lattices, similar straight vortex sheets configuration can also been observed in the pure harmonic trap [29,30]. However, in that case, the intercomponent and intracomponent interaction strengths are required to be nearly equal, so the parameter region of this phase is extremely narrow. At the same time, the straight vortex sheets are unstable as there exist many different metastable bent vortex sheet configurations with almost the same energy as the straight one. This is because the energy of the vortex sheets is mainly determined by two factors, the intervortex spacing within a vortex sheet and the intersheet spacing. The shape of the vortex sheets has slight influence on the energy of the system. Thus, it is easy for the straight vortex sheets to bend under external disturbances. In contrast, when the spin-dependent optical lattices are present, the shape of the vortex sheets becomes an important factor in determining the energy of the system, and any bending in the straight vortex sheets will cost much energy. So the straight half-vortex sheets configuration obtained in our system can be maintained stably. In our imaginary-time propagations, for any trial initial configurations, the straight vortex sheets configuration is always uniquely obtained after sufficient convergence of the energy. In addition, this configuration does not face the intracomponent interaction strength limitations. Although the intercomponent and intracomponent interaction strengths, which are chosen in Fig. 2, happen to be approximately equal, we find that for a large difference between intercomponent and intracomponent interaction strengths, stable straight vortex sheets configuration can also be obtained.

Next, we study the unique superfluid velocity behavior of this structure. The most well-known character of a vortex sheet is the discontinuity of the tangential component of the velocity

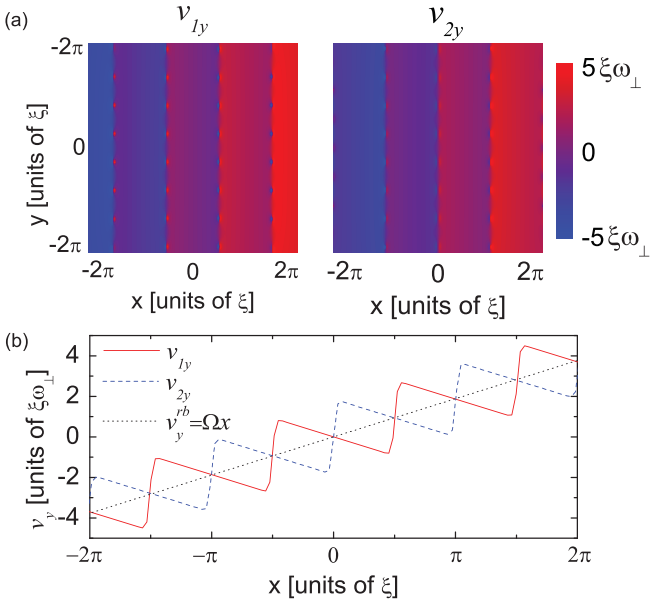

FIG. 3. (Color online) (a) The tangential components v_{1y} (left) and v_{2y} (right) of the superfluid velocities $\mathbf{v}_1$ and $\mathbf{v}_2$ of the two states for $\Omega = 0.6\omega_\perp$ and $T = \pi\xi$. (b) Section views of v_{1y} (solid line) and v_{2y} (dashed line) along the x axis. The y component $v_y^{\rm rb} = \Omega x$ of the rigid body rotation velocity $\mathbf{v}^{\rm rb}$ is shown by the dotted line for comparison.

across the sheet. The regular arrangement of the straight vortex sheets allows us to observe this phenomenon clearly. In Fig. 3(a), the tangential components (the components along the y axis) v_{1y} and v_{2y} of the superfluid velocities $\mathbf{v}_1$ and $\mathbf{v}_2$ of the two states are presented. We can see that both v_{1y} and v_{2y} discontinuously jump across every sheet. In order to describe the tangential velocities in detail, the section views of v_{1y} and v_{2y} along the x axis are shown in Fig. 3(b). The y component $v_y^{\rm rb} = \Omega x$ of the rigid body rotation velocity $\mathbf{v}^{\rm rb} = \Omega \times \mathbf{r}$ is presented for comparison. We find that both the tangential velocities v_{1y} and v_{2y} have a sawtoothlike change following the rigid-body value $v_y^{\rm rb}$. The value of v_{iy} jumps $2\Omega b$ across the sheet in each component and then decreases Ωb linearly in an intersheet spacing b. Here, the intersheet spacing b is defined as the length between two neighboring sheets in the same component.

The numerical results obtained above can be understood analytically. Considering that the y component of the rigid body rotation velocity is $v_y^{\rm rb} = \Omega x$, which is independent of y, we suppose that the tangential components of the superfluid velocity on both sides of the sheet v_{iy}^- and v_{iy}^+ are also independent of y. According to Onsager-Feynman quantization condition [5]

$$\oint_{\mathcal{C}} \mathbf{v}_{\rm s} \cdot d\mathbf{l} = \frac{2\pi\hbar}{m} N_v, \tag{5}$$

if we choose the two sides of the sheet as the integration path, we can calculate that the tangential velocity jump across a sheet is

$$\Delta v_{iy} = v_{iy}^+ - v_{iy}^- = \frac{2\pi\hbar}{m}\frac{1}{d_v}, \tag{6}$$

where d_v is the intervortex spacing within a vortex sheet. This implies that the tangential velocity jump across the sheet is only determined by the intervortex spacing within the sheet. According to the Feynman relation, the mean vortex density of each component can be estimated as

$$n_1 = n_2 = \frac{m\Omega}{\hbar\pi}, \tag{7}$$

so we can obtain that the intervortex spacing within a vortex sheet is

$$d_v = \frac{\pi\hbar}{m\Omega T}. \tag{8}$$

Substituting Eq. (8) into Eq. (6), we have

$$\Delta v_{iy} = 2\Omega T. \tag{9}$$

Equation (9) suggests that the velocity jump can be accurately controlled by adjusting the rotating angular frequency Ω and the period of the optical lattice potential T. As the intersheet spacing b is just equal to the period of the optical lattice potential T, the tangential velocity jump across the sheet can also be expressed as

$$\Delta v_{iy} = 2\Omega b. \tag{10}$$

Meanwhile, in order to follow the rigid-body value v_y^{rb}, v_{iy} must decrease Ωb in an intersheet spacing. These analytical results agree well with the numerical simulations above.

Further numerical simulations with different choices of computational parameters in Eq. (4) show that the straight half-vortex sheets can also be obtained in any other two-component BEC system consisting of two hyperfine spin states. For example, a two-level ^{23}Na BEC system with $|F = 1, m_f = 1\rangle$ and $|F = 1, m_f = 0\rangle$. In addition, for the case of a two-component BEC system consisting of different atomic species, as the atomic masses of the two components are unequal, the vortex densities of the two components will differ from one another. We expect that more complicated straight half-vortex sheet structures, with the sheets of different components carrying a different number of vortices, would be obtained.

IV. DOMAIN-WALL TRAINS

The spinor order parameter of the two-component BECs allows us to analyze this system as a pseudospin-1/2 BEC and take it as a magnetic system [35]. Introducing a normalized complex-valued spinor $\boldsymbol{\chi}$, we represent the two-component wave functions as $\psi_i = \sqrt{\rho_T(\mathbf{r})}\chi_i(\mathbf{r})$, where $\rho_T(\mathbf{r})$ is the total density and the spinor satisfies $|\chi_1|^2 + |\chi_2|^2 = 1$. In pseudospin representation, the pseudospin density is defined as $\mathbf{S} = \boldsymbol{\chi}^{\mathbf{T}}\boldsymbol{\sigma}\boldsymbol{\chi}$, where $\boldsymbol{\sigma}$ is the Pauli matrix. Then we have

$$S_x = 2|\chi_1||\chi_2|\cos(\theta_1 - \theta_2), \tag{11a}$$

$$S_y = -2|\chi_1||\chi_2|\sin(\theta_1 - \theta_2), \tag{11b}$$

$$S_z = |\chi_1|^2 - |\chi_2|^2, \tag{11c}$$

where θ_i is the phase of the wave function ψ_i.

As the presence of the spin-dependent optical lattices, the two-component BECs are phase separated and a train of domain walls are formed naturally at the interfaces of the two components. By the pseudospin representation, we investigate the response of the domain walls to rotation. In order to reveal the essential influence of the rotation on the structure of the domain walls, the nonrotating and rotating ground states of the two-component condensates are calculated under the same parameters. As the rotation can create an effective harmonic centrifugal potential with frequency Ω [42], we change the radial harmonic trapping frequency to $\sqrt{\omega_\perp^2 - \Omega^2}$ in the absence of rotation. Thus, the nonrotating ground-state density distribution is nearly the same as the rotating ground-state density distribution, except that no vortex is created in the low-density regions of each component in the nonrotating ground state.

The vectorial representation of the pseudospin $\mathbf{S}$ for the nonrotating and rotating ground states are presented in Figs. 4(a) and 4(b), respectively. Correspondingly, the pseudospin densities S_x, S_y, and S_z are presented in Fig. 5. From Figs. 4 and 5, we can see that two distinct types of domain walls, with their magnetic moments reversing in different manners, are formed at the interfaces of the spin up ($S_z = 1$) and spin down ($S_z = -1$) domains. In the absence of rotation, the magnetic moments on the domain walls reverse only along the x axis [see Fig. 4(a)], and the pseudospin density $S_y = 0$ [see the upper panels of Fig. 5]. Therefore, this type of domain wall is the classical Néel wall. In contrast, in the presence of rotation, the magnetic moments on the domain walls do not only reverse along the x axis, but twist and form spatially periodic eyebrowlike spin textures [see Fig. 4(b) and the lower panels of Fig. 5]. This domain wall, with its unique manner of magnetic moment reverse, has not been observed in common magnetic materials. It is the product of the phase-separated two-component BECs in response to external rotation, and reflects the influence of rotation on the magnetism of BECs.

It should be indicated that the classical Néel wall does not carry topological charges. However, the twist of the magnetic moments makes the domain wall carry topological charges. According to the topological charge density

$$q(\mathbf{r}) = \frac{1}{8\pi}\epsilon^{ij}\mathbf{S}\cdot\partial_i\mathbf{S}\times\partial_j\mathbf{S}, \tag{12}$$

we can calculate that each period of the eyebrowlike spin textures on the domain wall just carries one unit topological charge. As shown in Figs. 4 and 5, from the distributions of the vortices and the spin textures, we can see that the number of the vortices is just half the number of the topological charges.

Next, we fasten our attention on the structure of the eyebrowlike spin textures. From Eq. (11a) and Eq. (11b), the direction that the magnetic moments reverse along just depends on the relative phase, and can be represented by an azimuthal angle

$$\alpha = \theta_2 - \theta_1. \tag{13}$$

An amplification of Fig. 4(b) for one period is presented in Fig. 6(a). From Fig. 6(a), we can see that the azimuthal angle of the magnetic moments changes from $-\pi$ to π along the domain wall in a period, but it is constant along the normal direction of the domain wall.

It is instructive to project the pseudospin density vector $\mathbf{S}$ onto the surface of a unit Bloch sphere [see Fig. 6(b)]. Topologically, the topological charge counts the times that the Bloch sphere is covered. So one texture just covers the Bloch

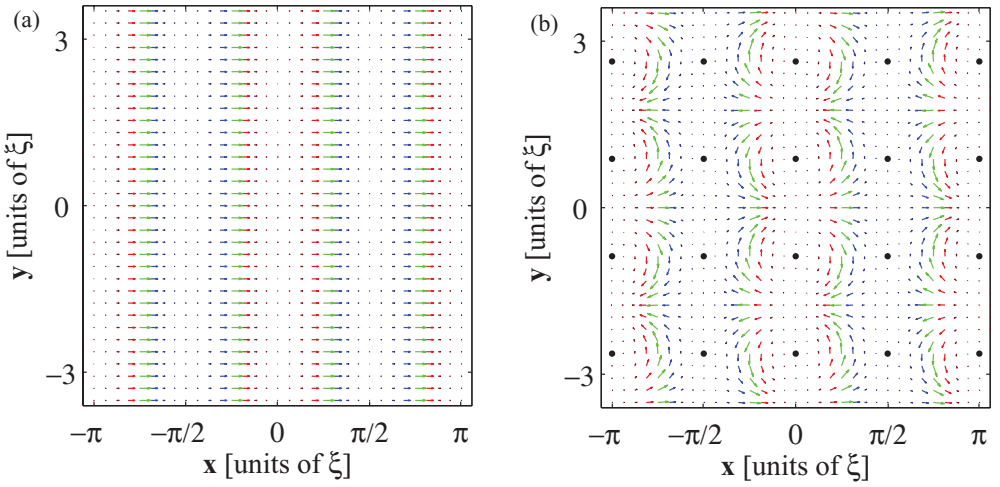

FIG. 4. (Color online) The vectorial representations of the pseudospin **S** projected onto the x-y plane for (a) $\Omega = 0$, $T = \pi\xi$, and (b) $\Omega = 0.6\omega_\perp$, $T = \pi\xi$. The colors ranging from blue to red describe the values of S_z from -1 to 1. The locations of the vortices are marked by black dots (•).

sphere once. From Fig. 6, we find that walking through the domain wall from one side to the other corresponds to strolling along a longitude line of the Bloch sphere from one pole to the other, and walking along the domain wall corresponds to strolling along a latitude line of the Bloch sphere. This is different from the case of a skyrmion, for which walking along the radial direction of the skyrmion corresponds to strolling along the longitude line of the Bloch sphere, and walking along the azimuthal direction of the skyrmion corresponds to strolling along the latitude line of the Bloch sphere. Therefore, this eyebrowlike spin texture essentially corresponds to a skyrmion in the polar coordinates instead of the Cartesian ones.

We reveal the formation mechanism of the spatially periodic eyebrowlike spin textures on the domain walls. In the absence of rotation, there is no relative phase between the two components and the azimuthal angle $\alpha = 0$. The magnetic moments on the domain walls only reverse along the x axis. Therefore, the domain walls are classical Néel walls. In the presence of rotation, straight vortex sheets are created in the two components and arranged alternately on two sides of the domain walls. These alternately arranged vortex sheets induce a linear gradient of the relative phase along the domain walls [see Fig. 7]. So the azimuthal angle α can be approximatively expressed as

$$\alpha = \mathcal{P}(\kappa y), \tag{14}$$

where $\mathcal{P}$ projects the angle κy onto $(-\pi,\pi]$ and κ is a constant coefficient, which describes the spatial change frequency of the azimuthal angle. The value of κ will be given in the next section. From Eq. (14), the azimuthal angle of the magnetic moments on the domain walls changes periodically along the y direction, and spatially periodic eyebrowlike spin textures are formed. This suggests that the spatially periodic

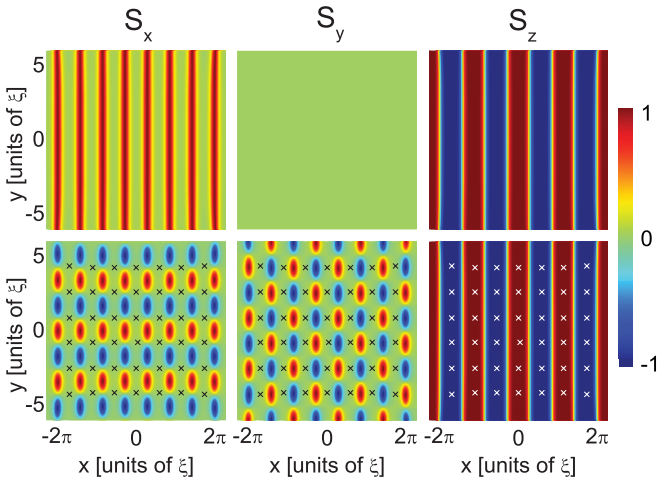

FIG. 5. (Color online) The pseudospin densities S_x (left), S_y (middle), and S_z (right). The upper panels show the case of $\Omega = 0$ and $T = \pi\xi$, and the lower panels show the case of $\Omega = 0.6\omega_\perp$ and $T = \pi\xi$. The locations of the vortices are marked by crosses (×).

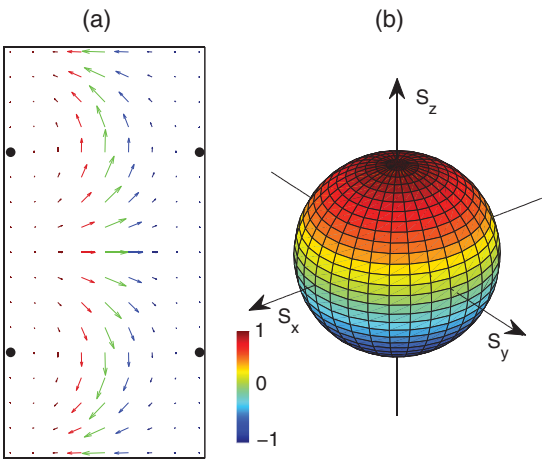

FIG. 6. (Color online) (a) An amplification of Fig. 4(b) in one period. (b) Bloch sphere of the pseudospin density vector **S**. Values of S_z are represented by linear levels from blue to red (-1 to 1).

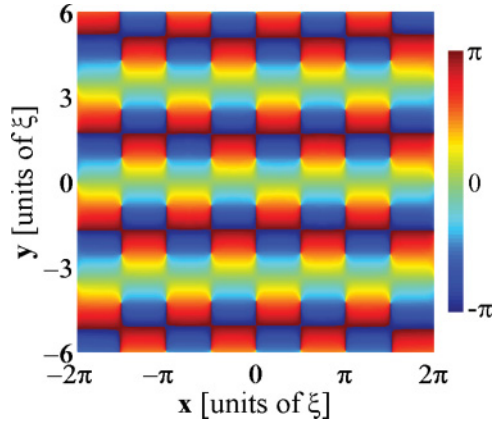

FIG. 7. (Color online) The relative phase $\theta_1 - \theta_2$ for $\Omega = 0.6\omega_\perp$ and $T = \pi\xi$, where θ_1 and θ_2 are the phases of the wave functions ψ_1 and ψ_2, respectively.

eyebrowlike spin textures on the domain walls result from the linear gradient of the relative phase, which is induced by the alternating arrangement of the straight vortex sheets in the two components. In general, there are two factors determining the emergence of the eyebrowlike spin textures in two-component BECs: the domain walls and the linear gradient of the relative phase along them. We predict that the eyebrowlike spin textures would also be observed on the domain walls in other phase-separated rotating two-component BECs.

V. TEXTURE CONTROL

In this section, we discuss the influences of the system parameters on the eyebrowlike spin textures. Firstly, we study the distribution of the textures analytically. The topological charge density q has another formulation derived from the effective velocity [43]

$$q(\mathbf{r}) = \frac{m}{2\pi\hbar}(\nabla \times \mathbf{v}_{\rm eff})_z , \tag{15}$$

where the effective velocity is defined as

$$\mathbf{v}_{\rm eff} = \frac{(\rho_1\mathbf{v}_1 + \rho_2\mathbf{v}_2)}{\rho_T}, \tag{16}$$

with ρ_i the density of each component. Approximately treating the effective velocity $\mathbf{v}_{\rm eff}$ as the classical rigid body value $\mathbf{v}_{\rm rb} = \Omega \times \mathbf{r}$, we obtain the mean topological charge density

$$\bar{q} = \frac{m\Omega}{\pi\hbar}. \tag{17}$$

From Eq. (17), we can calculate that the topological charge on a domain wall per unit length is

$$\eta_q = \frac{m\Omega T}{2\pi\hbar}. \tag{18}$$

This implies that the number of the textures carried by a domain wall is proportional to the rotating angular frequency Ω and the period of the optical lattice potential T. Thus, an accurate control on the texture number can be realized by adjusting the rotating angular frequency and the period of the optical lattices.

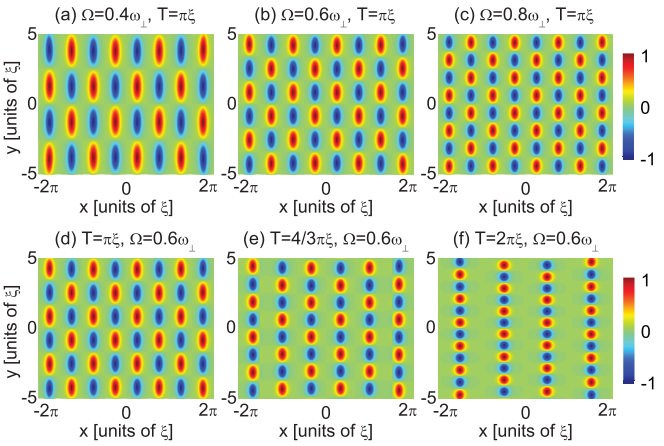

FIG. 8. (Color online) The pseudospin density S_y for different rotating angular frequencies Ω and periods of the optical lattice potential T. The upper panels show S_y for $T = \pi\xi$ with (a) $\Omega = 0.4\omega_\perp$, (b) $\Omega = 0.6\omega_\perp$, and (c) $\Omega = 0.8\omega_\perp$. The lower panels show S_y for $\Omega = 0.6\omega_\perp$ with (d) $T = \pi\xi$, (e) $T = 4/3\pi\xi$, and (f) $T = 2\pi\xi$.

From Eq. (18), the spatial change frequency κ of the azimuthal angle α in Eq. (14) can be calculated as

$$\kappa = 2\pi\eta_q = \frac{m\Omega T}{\hbar}. \tag{19}$$

Thus, we obtain the azimuthal angle

$$\alpha = \mathcal{P}\left(\frac{m\Omega T}{\hbar}y\right). \tag{20}$$

In order to verify the above analytical discussion, we perform numerical simulations. The pseudospin density S_y for different rotating angular frequencies Ω with constant period of the optical lattice potential T is shown in the upper panels of Fig. 8, and S_y for different T with constant Ω is shown in the lower panels. Obviously, the number of the topological charges carried by a domain wall increases in direct proportion with the increase of Ω and T. For quantitative comparison, we choose $\Omega = 0.6\omega_\perp$ and $T = \pi\xi$ as an example. From Eq. (18), we can calculate that the number of the textures on a domain wall in the region of $y = [-5\xi, 5\xi]$ is 3. This agrees well with the result of the numerical simulation in Fig. 8(b).

In our system, as the presence of the spin-dependent optical lattices, the two components are always phase separated and not subject to the immiscible condition, $g_{12}^2 > g_{11}g_{22}$ [44]. Even so, the intercomponent interaction g_{12} has an important influence on the domain wall width. When g_{12} is small, the two components prefer to have larger overlap at the interfaces, so the domain walls are wider. Contrarily, when g_{12} is increased, the enhanced immiscibility makes the overlap of the two components reduced, so the domain walls become narrower. To illustrate this point, the cross section views of S_z along the x axis for different intercomponent scattering length a_{12} with constant intracomponent scattering lengths a_{11} and a_{22} are shown in Fig. 9(b). We can see that the domain wall width is sensitive to the intercomponent interaction, and with

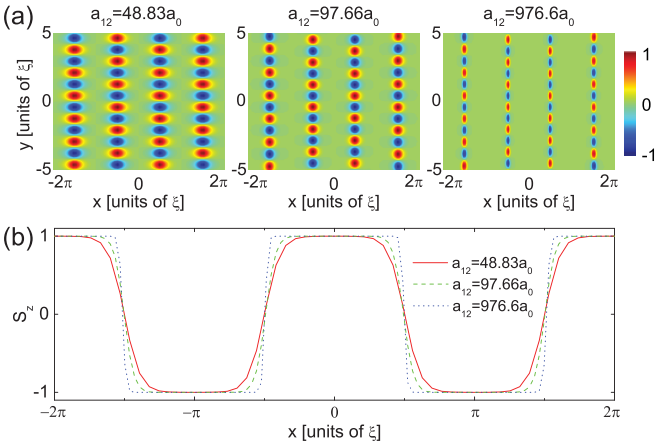

FIG. 9. (Color online) (a) The pseudospin density S_y for the intercomponent scattering length $a_{12} = 48.83a_0$ (left), $97.66a_0$ (middle), and $976.6a_0$ (right) with the intracomponent scattering lengths $a_{11} = 100.40a_0$ and $a_{22} = 95.00a_0$, $\Omega = 0.6\omega_\perp$ and $T = 2\pi\xi$. (b) Cross section views of S_z along the x axis for $a_{12} = 48.83a_0$ (solid line), $97.66a_0$ (dashed line), and $976.6a_0$ (dotted line).

increasing the strength of intercomponent interaction, the domain walls become narrow. Moreover, the corresponding pseudospin densities S_y with the same parameters as Fig. 9(b) are plotted in Fig. 9(a). We find that the eyebrowlike spin textures are always embedded on the domain walls and the texture width changes with the width of the domain walls. This suggests that we can control the texture width by adjusting the width of the domain wall. In a word, both the influences of the system parameters on the number and width of the eyebrowlike spin textures provide basis for texture control in this system.

VI. DYNAMICAL BEHAVIORS UNDER EXTERNAL DISTURBANCES

In this section, we discuss the dynamics of this system under external disturbances. Taking the ground state obtained in Fig. 2 as an initial value and employing a Gaussian noise, we perform real-time dynamic evolutions of Eq. (4). The density profile of the ψ_1 component at $t = 10^3\omega_\perp^{-1}$ is plotted in Fig. 10. From the density profile, we can see that the straight half-vortex sheet configuration is stable and robust with respect to external disturbances. This is agree with our previous analysis in Sec. III.

With further observations on the actions of the vortices by tracing their trajectories, we find that all the vortices on each sheet are moving collectively at a constant velocity with the interspace of them maintained. When a vortex is created and enters into the sheet from one side, the vortex on the other side leaves out and annihilates. The total number of the vortices is conserved. This phenomenon is intuitively illuminated in Fig. 10 by indicating the direction and magnitude of the velocities of all the vortices. We understand this dynamical behavior of the vortex sheets by noting that the Gaussian noise brings small amounts of energy to the system. This additional energy is so little that it can not change the density distribution of condensates. However, as the vortices are located in the extremely low-density regions, the movement of them just

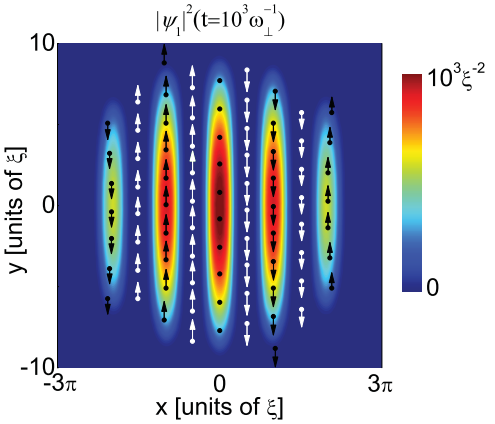

FIG. 10. (Color online) The density profile of ψ_1 at $t = 10^3\omega_\perp^{-1}$ of the real-time dynamical evolution with the same parameters as Fig. 2. The initial value is chosen as the ground state in Fig. 2 plus a Gaussian noise of level 0.5%. The vortices of both the two components are marked by dots (•), and arrows are added to show the direction and magnitude of the velocities of the vortex move.

need little energy cost. So the energy from the noise can excite the movement of the vortices easily. At the same time, because of the strong interaction between the neighboring vortices in the same sheet, the interspace of the vortices keeps almost invariable. By numerical simulations, we have confirmed that this collective movement of the vortices can happen stably without experiencing any significant nonlinear decay.

In pseudospin representation, the direct effect of the collective movement of the vortices is to cause the propagation of the eyebrowlike spin textures along the domain walls. Under the same disturbances as Fig. 10, the time evolution of the pseudospin density S_x on a domain wall is shown in Fig. 11. We can see that the spin-wave propagates along the domain wall at a constant velocity. This implies that, for a fixed point in space, the local spin is precessing around the S_z axis at a constant angle. This corresponds to strolling constantly along a latitude line on the Bloch sphere [see Fig. 12(b)]. As an

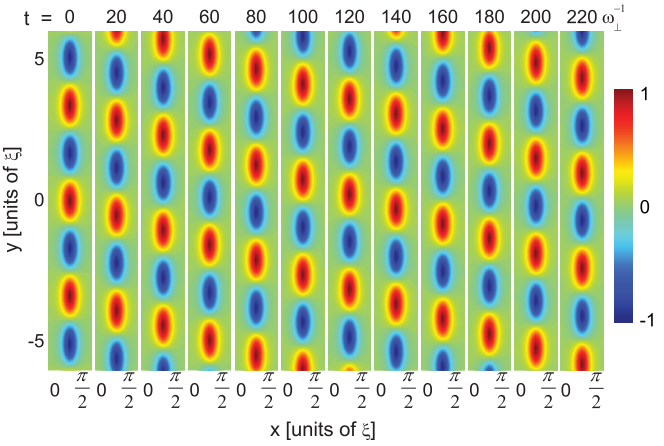

FIG. 11. (Color online) Time evolution of the pseudospin density S_x in a domain wall at the region of $[0, \frac{\pi}{2}, -6, 6]$ in the presence of a Gaussian noise of level 0.5%. The numerical simulation process is the same as Fig. 10.

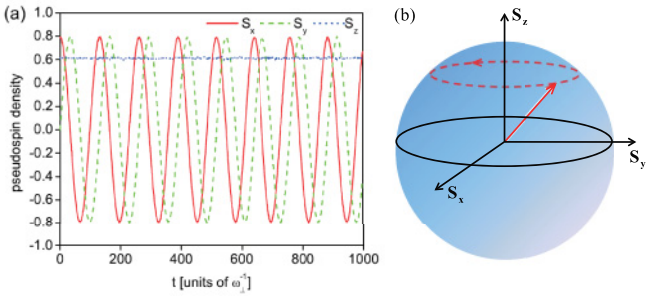

FIG. 12. (Color online) (a) Time evolution of the pseudospin S_x, S_y, and S_z at a fixed point ($x = 0.63625\xi$, $y = 0$) in the presence of a Gaussian noise at level 0.5. (b) Bloch sphere showing the procession of the local spin at a fixed point in space (the red dashed line on Bloch sphere highlights spin trajectory).

example, with the same numerical simulation progress, the time evolution of the local spin at ($x = 0.65625\xi$, $y = 0$) is shown in Fig. 12(a). We can see that the S_z component of the pseudospin keeps invariable, while the S_x and S_y components vary periodically following the sine and cosine functions, respectively.

In the present study, we have only discussed the influence of the Gaussian noise on the dynamics behavior of this system. It should be indicated that the straight half-vortex sheet configuration is still robust under other external disturbances, for example, slight trap inhomogeneities. Meanwhile, the collective movement of the vortices and the spin-wave propagation, as well as the local spin precession, can also be observed in that case.

VII. CONCLUSION

We have investigated half-vortex sheets and domain-wall trains of rotating two-component BECs in spin-dependent optical lattices. A stable vortex structure named straight half-vortex sheets is obtained. The stability of this vortex structure is due to the peculiar use of the 1D spin-dependent optical lattices. The unique superfluid velocity behavior of this system is studied both numerically and analytically. We find that the tangential component of the superfluid velocity always discontinuously jumps across every sheet. The value of the jump is essentially determined by the intervortex spacing within the sheet, and can be adjusted by changing the rotating angular frequency and the period of the optical lattices.

As the presence of the spin-dependent optical lattices, a train of domain walls are formed naturally at the interfaces of the two components. We have investigated the response of the domain wall to rotation, and found that in response to rotation, the magnetic moments on the domain walls twist and form spatially periodic eyebrowlike spin textures. One period of the eyebrowlike spin textures has the same topological charge as a skyrmion, but their structures are distinctly different. We described the structure of the spin texture in detail by projecting it on a Bloch sphere. We have revealed that there are two factors determining the emergence of the eyebrowlike spin textures in two-component BECs: the domain walls and the linear gradient of the relative phase along them. In the present system, the linear gradient of the relative phase is induced by the alternating arrangement of the vortex sheets. It should be emphasized that the appearance of the eyebrowlike spin textures in response to rotation is a characteristic feature of domain wall in two-component BECs, and in other phase-separated rotating systems eyebrowlike spin textures would also be observed on the domain walls.

We have investigated the influences of the system parameters on the textures and find that the number of the textures on a domain wall is proportional to the rotating angular frequency and the period of the optical lattices. Meanwhile, the numerical results indicate that these eyebrowlike spin textures are always embedded on the domain walls and the texture width changes with the width of the domain walls. Their width can be controlled by adjusting the intercomponent interaction strength. These allow us to realize accurate texture control.

Under external disturbances, we have observed the collective movement of the vortices along the sheet and the spin-wave propagation along the domain wall. At the same time, the propagation of the spin wave along the domain wall results in local spin precession around the S_z axis. These interesting dynamical behaviors may be associated with certain low-energy excitation modes, and could be further analyzed by the Bogoliubov excitation spectrum.

For the experimental observation of the structure obtained in the present work, the density is the most direct observable. However, as the vortices are all hidden in the low-density regions, one can not strictly confirm the occurrence of this vortex structure from the density images. Fortunately, as discussed in Fig. 5, the vortices are always embedded in the spatially periodic pseudospin density field. The unique patterns of the transverse components S_x and S_y of the pseudospin density provide us an excellent evidence for the occurrence of this phase. So we suggest that the pseudospin density is the best observable to show the smoking gun for the occurrence of the phase. With the development of the magnetization-sensitive phase-contrast imaging technique [45], both the longitudinal and transverse components of the pseudospin density can be imaged nondestructively with high spatial resolution [18,46]. We expect that the straight half-vortex sheets and the spatially periodic eyebrowlike spin textures on the domain walls, as well as their dynamical behaviors under external disturbances, would be observed in the future experiments.

ACKNOWLEDGMENTS

We are grateful to D.-S. Wang and S.-W. Song for stimulating discussions and valuable suggestions. This work was supported by the National Key Basic Research Special Foundation of China (NKBRSFC) under Grants No. 2011CB921502, No. 2012CB821305, No. 2009CB930701, and No. 2010CB922904; the National Natural Science Foundation of China (NSFC) under Grants No. 10972125, No. 10934010, and No. 60978019; the NSFC and the Research Grants Council of Hong Kong Joint Research Scheme (NSFC-RGC) under Grants No. 11061160490 and No. 1386-N-HKU748/10; the Natural Science Foundation of Shanxi Province (NSFSP) under Grant No. 2010011001-2, and the Special Foundation for Returnee of Shanxi Province (SFRSP).

[1] W. F. Vinen and J. J. Niemela, J. Low Temp. Phys. **128**, 167 (2002); M. Tsubota, J. Phys.: Condens. Matter **21**, 164207 (2009).

[2] S. S. P. Parkin, M. Hayashi, and L. Thomas, Science **320**, 190 (2008); M. Hayashi, L. Thomas, R. Moriya, C. Rettner, and S. S. P. Parkin, *ibid*. **320**, 209 (2008).

[3] U. K. Rößler, A. N. Bogdanov, and C. Pfleiderer, Nature (London) **442**, 797 (2006); X. Z. Yu, Y. Onose, N. Kanazawa, J. H. Park, J. H. Han, Y. Matsui, N. Nagaosa, and Y. Tokura, *ibid*. **465**, 901 (2010).

[4] T. Schulz, R. Ritz, A. Bauer, M. Halder, M. Wagner, C. Franz, C. Pfleiderer, K. Everschor, M. Garst, and A. Rosch, Nature Phys. **7**, 713 (2011).

[5] A. L. Fetter and A. A. Svidzinsky, J. Phys.: Condens. Matter **13**, R135 (2001); N. R. Cooper, Adv. Phys. **57**, 539 (2008); A. L. Fetter, Rev. Mod. Phys. **81**, 647 (2009).

[6] D. V. Freilich, D. M. Bianchi, A. M. Kaufman, T. K. Langin, and D. S. Hall, Science **329**, 1182 (2010).

[7] D. M. Jezek and H. M. Cataldo, Phys. Rev. A **83**, 013629 (2011).

[8] D.-S. Wang, S.-W. Song, B. Xiong, and W. M. Liu, Phys. Rev. A **84**, 053607 (2011).

[9] K. Kasamatsu, M. Tsubota, and M. Ueda, Int. J. Mod. Phys. B **19**, 1835 (2005); M. Ueda and Y. Kawaguchi, e-print arXiv:1001.2072v2; M. Tsubota, K. Kasamatsu, and M. Kobayashi, e-print arXiv:1004.5458v2.

[10] G. W. Semenoff and F. Zhou, Phys. Rev. Lett. **98**, 100401 (2007).

[11] A.-C. Ji, W. M. Liu, J. L. Song, and F. Zhou, Phys. Rev. Lett. **101**, 010402 (2008).

[12] M. Eto, K. Kasamatsu, M. Nitta, H. Takeuchi, and M. Tsubota, Phys. Rev. A **83**, 063603 (2011).

[13] S.-W. Su, C.-H. Hsueh, I.-K. Liu, T.-L. Horng, Y.-C. Tsai, S.-C. Gou, and W. M. Liu, Phys. Rev. A **84**, 023601 (2011).

[14] S. Coen and M. Haelterman, Phys. Rev. Lett. **87**, 140401 (2001).

[15] D. T. Son and M. A. Stephanov, Phys. Rev. A **65**, 063621 (2002).

[16] P. G. Kevrekidis, B. A. Malomed, D. J. Frantzeskakis, and A. R. Bishop, Phys. Rev. E **67**, 036614 (2003); P. G. Kevrekidis, H. Susanto, R. Carretero-González, B. A. Malomed, and D. J. Frantzeskakis, *ibid*. **72**, 066604 (2005).

[17] B. A. Malomed, H. E. Nistazakis, D. J. Frantzeskakis, and P. G. Kevrekidis, Phys. Rev. A **70**, 043616 (2004).

[18] L. E. Sadler, J. M. Higbie, S. R. Leslie, M. Vengalattore, and D. M. Stamper-Kurn, Nature (London) **443**, 312 (2006).

[19] J. Jin, S. Zhang, and W. Han, J. Phys. B **44**, 165302 (2011).

[20] S. Yi and H. Pu, Phys. Rev. Lett. **97**, 020401 (2006).

[21] G. Ruben, M. J. Morgan, and D. M. Paganin, Phys. Rev. Lett. **105**, 220402 (2010).

[22] J. A. M. Huhtamäki, M. Takahashi, T. P. Simula, T. Mizushima, and K. Machida, Phys. Rev. A **81**, 063623 (2010); J. A. M. Huhtamäki and P. Kuopanportti, *ibid*. **82**, 053616 (2010).

[23] T. Kawakami, T. Mizushima, and K. Machida, Phys. Rev. A **84**, 011607(R) (2011).

[24] S.-W. Su, I.-K. Liu, Y.-C. Tsai, W. M. Liu, S.-C. Gou, e-print arXiv:1111.6338v1.

[25] J. R. Abo-Shaeer, C. Raman, J. M. Vogels, and W. Ketterle, Science **292**, 476 (2001).

[26] E. J. Mueller and T.-L. Ho, Phys. Rev. Lett. **88**, 180403 (2002).

[27] K. Kasamatsu, M. Tsubota, and M. Ueda, Phys. Rev. Lett. **91**, 150406 (2003).

[28] V. Schweikhard, I. Coddington, P. Engels, S. Tung, and E. A. Cornell, Phys. Rev. Lett. **93**, 210403 (2004).

[29] S. J. Woo, S. Choi, L. O. Baksmaty, and N. P. Bigelow, Phys. Rev. A **75**, 031604(R) (2007).

[30] K. Kasamatsu and M. Tsubota, Phys. Rev. A **79**, 023606 (2009).

[31] P. Mason and A. Aftalion, Phys. Rev. A **84**, 033611 (2011).

[32] S.-J. Yang, Q.-S. Wu, S.-N. Zhang, and S. Feng, Phys. Rev. A **77**, 033621 (2008).

[33] P. Kuopanportti, J. A. M. Huhtamäki, and M. Möttönen, Phys. Rev. A **85**, 043613 (2012).

[34] T. Mizushima, N. Kobayashi, and K. Machida, Phys. Rev. A **70**, 043613 (2004).

[35] K. Kasamatsu, M. Tsubota, and M. Ueda, Phys. Rev. A **71**, 043611 (2005).

[36] K. Kasamatsu, M. Tsubota, and M. Ueda, Phys. Rev. A **67**, 033610 (2003).

[37] O. Mandel, M. Greiner, A. Widera, T. Rom, T. W. Hänsch, and I. Bloch, Phys. Rev. Lett. **91**, 010407 (2003); Nature (London) **425**, 937 (2003).

[38] K. M. Mertes, J. W. Merrill, R. Carretero-González, D. J. Frantzeskakis, P. G. Kevrekidis, and D. S. Hall, Phys. Rev. Lett. **99**, 190402 (2007).

[39] S. Burger, F. S. Cataliotti, C. Fort, F. Minardi, M. Inguscio, M. L. Chiofalo, and M. P. Tosi, Phys. Rev. Lett. **86**, 4447 (2001).

[40] F. Dalfovo and S. Stringari, Phys. Rev. A **53**, 2477 (1996); M. L. Chiofalo, S. Succi, and M. P. Tosi, Phys. Rev. E **62**, 7438 (2000).

[41] W. Bao, I.-L. Chern, and F. Y. Lim, J. Comput. Phys. **219**, 836 (2006).

[42] C. Raman, J. R. Abo-Shaeer, J. M. Vogels, K. Xu, and W. Ketterle, Phys. Rev. Lett. **87**, 210402 (2001).

[43] E. J. Mueller, Phys. Rev. A **69**, 033606 (2004).

[44] E. Timmermans, Phys. Rev. Lett. **81**, 5718 (1998).

[45] J. M. Higbie, L. E. Sadler, S. Inouye, A. P. Chikkatur, S. R. Leslie, K. L. Moore, V. Savalli, and D. M. Stamper-Kurn, Phys. Rev. Lett. **95**, 050401 (2005).

[46] M. Vengalattore, S. R. Leslie, J. Guzman, and D. M. Stamper-Kurn, Phys. Rev. Lett. **100**, 170403 (2008).